Synthesis and Crystal Chemistry of a New Manganite Member $Bi_{3.6}Sr_{12.4}Mn_8O_{28+\delta}$, $n = 2$ of the $[Bi_2Sr_2MnO_6]_n[Sr_8Mn_6O_{16+\delta}]$-Related "Tubular" Family

D. Pelloquin, C. Michel, A. Maignan, M. Hervieu, and B. Raveau

Laboratoire de Cristallographie et Sciences des Matériaux, ISMRA-Université de Caen, Boulevard du maréchal Juin, 14050 Caen Cedex, France

A manganite with a "tubular" structure derived from the 2201-type, $Bi_{3.6}Sr_{12.4}Mn_8O_{28+\delta}$, has been synthesized. Its complex crystal chemistry has been studied using XRD, ND, and HREM techniques. It crystallizes in an orthorhombic cell, space group *Pbnb*, with $a = 5.4946$ Å, $b = 23.595(1)$ Å, and $c = 23.580(1)$ Å. This structure can be described as an intergrowth, along b, of two types of (010) slices: "2201"-type slices $[Bi_2Sr_2MnO_6]$ that are two octahedra thick and manganese-deficient perovskite-related slices $[Sr_8Mn_6O_{16+\delta}]$ that are one octahedron thick. A similar stacking is observed along c, which endows the structure with a pseudotetragonal character. Another way to describe this structure is to consider criss-crossing layers of manganese polyhedra forming tubes, where the [BiO] rows are inserted, and oxygen-deficient pillars, built up of four Mn polyhedra. This phase represents the $n = 2$ member of a new "tubular" family $[Bi_2Sr_2MnO_6]_n[Sr_8Mn_6O_{16+\delta}]$. Intergrowth and shearing mechanisms arise along the b and c directions, in agreement with the pseudotetragonal character of the structure. The investigation of the transport and magnetic properties of this new manganite shows that it is an insulator and exhibits weak antiferromagnetism at low temperature ($\theta p = -650$ K); the high-temperature data evidence an effective magnetic moment of 4.7 μ_B characteristic of high-spin Mn^{3+} ($\mu_{th} = 4.9$ μ_B). © 1998 Academic Press

INTRODUCTION

The discoveries of superconductivity at high temperature in copper-based oxides more than 10 years ago (1), and more recently colossal magnetoresistance (CMR) properties in manganese-based oxides (2), have demonstrated that transition metal oxides represent a very promising source for new materials with optimized properties. Curiously these two classes of compounds exhibit a great similarity in spite of their fundamentally different physical properties. They both derive from the perovskite-type structure in which the transition element is characterized by a Jahn Teller effect and shows a mixed-valence Cu(II)–Cu(III) or Mn(III)–Mn(IV). Consequently in the two systems, one

obtains layered structures, intergrowths of perovskite and rock salt-type layers. This is the case of the bismuth cuprates and manganites, which only differ by the oxygen stoichiometry of their perovskite layers, leading to the formulas $Bi_2Sr_2Ca_{m-1}Cu_mO_{2m+4+\delta}$ (3–6) and $Bi_2(Sr,Ca)_{m+1}Mn_mO_{3m+3+\delta}$ (7, 19) respectively.

In the case of copper-based oxides, the formation of transverse slices, perpendicular to the copper layers, allows new compounds to be generated. These new compounds derive from the layered cuprates either by single or double shearing mechanisms forming the "collapsed" cuprates (8–10), or by more complex phenomena forming the "tubular" cuprates (11–13). In contrast, no collapsed- or tubular-type structure has been evidenced to date for manganites, in spite of the great analogy between the layered cuprates and manganites. This issue is of great interest for the study of the magnetic and transport properties of the manganese oxides. We have thus investigated the formation of such compounds in the system Bi–Sr–Mn–O. We report herein on the first manganite, $Bi_{3.6}Sr_{12.4}Mn_8O_{28+\delta}$, that exhibits a "tubular" structure. The complex crystal chemistry of this phase, which represents the only known $n = 2$ member of the "tubular" series $[Bi_2Sr_2MO_6]_n[Sr_8M_6O_{16+\delta}]$ ($M =$ Cu, Mn), is described from high resolution electron microscopy and neutron diffraction data.

EXPERIMENTAL PROCEDURE

The Bi–Sr–Mn–O system was investigated close to the ideal composition expected for an $n = 2$ member of the tubular-type oxides (13), that is, $Bi_4Sr_{12}Mn_8O_{28+\delta}$. Two types of starting mixtures were considered to prepare samples with the above nominal composition. A first method was to start from a mixture of Bi_2O_3, SrO_2, and Mn/Mn_2O_3 in various ratios in order to control the oxygen content. The precursors were weighted according to the chosen cationic composition, intimately ground in an agate mortar, and placed in an alumina finger. Next, the mixtures

278

were sealed in an evacuated silica ampoule. Unfortunately, in this method, impurities like $Bi_{2-x}Sr_{2-y}MnO_{6+\delta}$ and $Sr_5Mn_4(CO_3)O_{10}$ were systematically detected. A second method was to start from mixtures of Bi_2O_3, SrO, and Mn_2O_3. To avoid the carbonate contamination, SrO was initially prepared by decomposing SrO_2 or $Sr(OH)_2, 8H_2O$ at 1100°C, and stored in a dry box. This step was performed in a dry box. Then the compounds were heated to 1050°C, at 150° h^{-1}, kept at this temperature for 24 h, and cooled to room temperature, at 150°C h^{-1}.

The electron diffraction (ED) study was carried out using a JEOL 200CX electron microscope fitted with an eucentric goniometer ($\pm 60°$). The high resolution electron microscopy (HREM) was performed with a TOPCON 002B operating at 200 KV (point resolution of 1.8 Å). HREM image calculations were carried out with the Mac-Tempas multislice program. The two microscopes were equipped with EDX analyzers.

The initial structural model was refined first from powder X-ray diffraction (XRD) data, collected with a Philips vertical diffractometer (Cu$K\alpha$ radiation) in the range $6° \leq 2\theta \leq 110°$ by increments of 0.02° (2θ), and next from neutron diffraction (ND) data. The latter were collected at room temperature on D2B diffractometer ($\lambda = 1.5938$ Å) at the Institut Laue Langevin (Grenoble, France) over the angular range $0° < 2\theta < 140°$ with a step of 0.05° (2θ). The scattering lengths were 0.8532, 0.7020, 0.373, and 0.5803 (in 10^{-12} cm) for Bi, Sr, Mn, and O, respectively. All structural calculations were performed by profile analysis with the program Fullprof (version 3.2) (14).

RESULTS

Under the synthesis conditions mentioned above, a new phase in the Bi–Sr–Mn–O system was obtained. Pure samples were only obtained for δ close to 2, i.e., a nominal oxygen stoichiometry of 30 oxygens per formula unit.

Cell Parameters and Homogeneity Range

The reciprocal space for numerous crystallites was reconstructed, by tilting about the crystallographic axes. EDX analyses were systematically coupled. These first analyses showed that the new material exhibits an orthorhombic cell with $a \approx a_p\sqrt{2} \approx 5.5$ Å (a_p is the parameter of the cubic perovskite-type structure) and $b \approx c \approx 23.6$ Å $\approx c_{2201}$ (c_{2201} being the periodicity of the layer stacking in the 2201-type structures). The conditions limiting the reflections are $hkl: h + k, k + 1, l + h = 2n$, compatible with the space groups $Fmmm$ and $Fmm2$. The superstructure reflections are rather intense and lie in commensurate positions, contrary to what is observed in the 2201-compound, $Bi_2Sr_2MnO_{6+\delta}$ (7), which exhibits an incommensurate modulated structure with a periodicity $b = q.a_p\sqrt{2}$ ($q \approx 4.9$). The [100] and [010] ED patterns are given in Fig. 1.
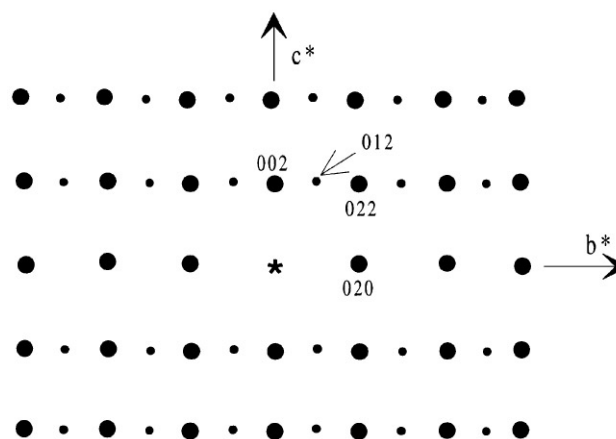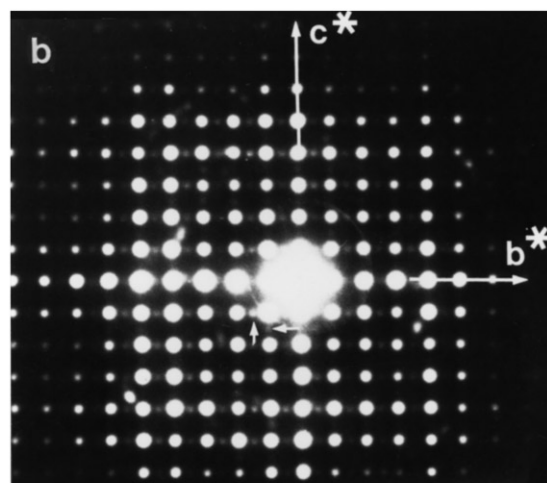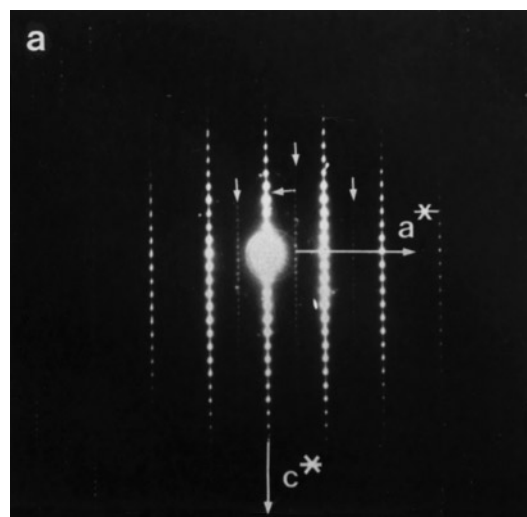
FIG. 1. (a) [010] and (b) [100] ED patterns. Extra reflections violating the F-type conditions are indicated by small white arrows on the experimental and schematic [100] patterns.

However, in most of the crystallites, in addition to the intense reflections characteristic of the F-type lattice, a second system of very weak reflections is observed, which

implies that the F-type conditions are violated. These weak reflections obey only the conditions $0kl : k = 2n$, $hk0 : k = 2n$ and $h0l$, $h + l = 2n$, compatible with the space group $Pbnb$. They are indicated by small white arrows in Figs. 1a and 1b. Their relative arrangement gives evidence for the existence of twinning domains, as the [010] and [001] variants are systematically superposed; this is clearly seen in Fig. 1b.

The EDX analyses show that the Sr/Bi ratio is slightly higher than the theoretical value, i.e., 3.4 instead of 3, leading to the actual composition $Bi_{3.6}Sr_{12.4}Mn_8O_x$. The XRD diffraction pattern is given in Fig. 2. The refinement of cell parameters in the space group $Pbnb$ led to $a = 5.4946(1)$ Å, $b = 23.595(1)$ Å, and $c = 23.580(1)$ Å. Note that the c parameter is very close to that previously refined for the Mn-based 2201-type compound (7).

For the characterization of this new structure, we have first considered the average structure, i.e., the F-type lattice. In a second step, we have taken into consideration the neutron diffraction data and the actual P-type lattice in order to understand the origin of the symmetry lowering and to clarify the oxygen positions in the pillars. Finally, local features and defects are discussed in order to understand the structural mechanisms that govern the structure.

The Average Structure

The origin of the superstructure along **b** was studied by high resolution electron microscopy, selecting [100] oriented crystals. A typical image is given in Fig. 3a, where the zones of high electron density are imaged as bright dots. The contrast consists in a regular paving of 4×4 bright dots squares, separated by perpendicular criss-crossing rows of gray dots. Referring to the HREM images recorded for the 2201-type compounds (18) and the "tubular" phases (12, 13), the intense bright dots are correlated to the positions of Bi and Sr atoms and the gray ones to the manganese positions. The great similarity of these images to those previously observed for the "tubular" cuprates (12, 13) allows a first approach to a structural model to be proposed.

In this model (Fig. 3b), the structure consists in the intergrowth, along **b**, of two types of (010) slices. The first slice exhibits the 2201-type structure, $Bi_2Sr_2MnO_{6+\delta}$, and is two Mn octahedra wide. The second is a perovskite-related slice, $[Sr_8Mn_6O_{16+\delta}]$. In that way, this new structure is characteristic of the "tubular-2" structure. Referring to the general formulation proposed for members of the "tubular" family (13), its ideal composition would be $[Bi_2Sr_2Mn O_{6\pm\delta}]_2[Sr_8Mn_6O_{16\pm\delta}]$, i.e., $Bi_4Sr_{12}Mn_8O_{28\pm\delta}$, which is close to the actual cationic composition, $Bi_{3.6}Sr_{12.4}Mn_8$, obtained by EDX. The spectacular characteristic of this $n = 2$ member of the "tubular" family is that the layer stacking sequence, that is, the 2201-type mode, is formed along two perpendicular directions, **b** and **c**. Note that this framework and these cell parameters were predicted previously (13), but the compound was never stabilized in the Bi–Sr–Cu–O system.

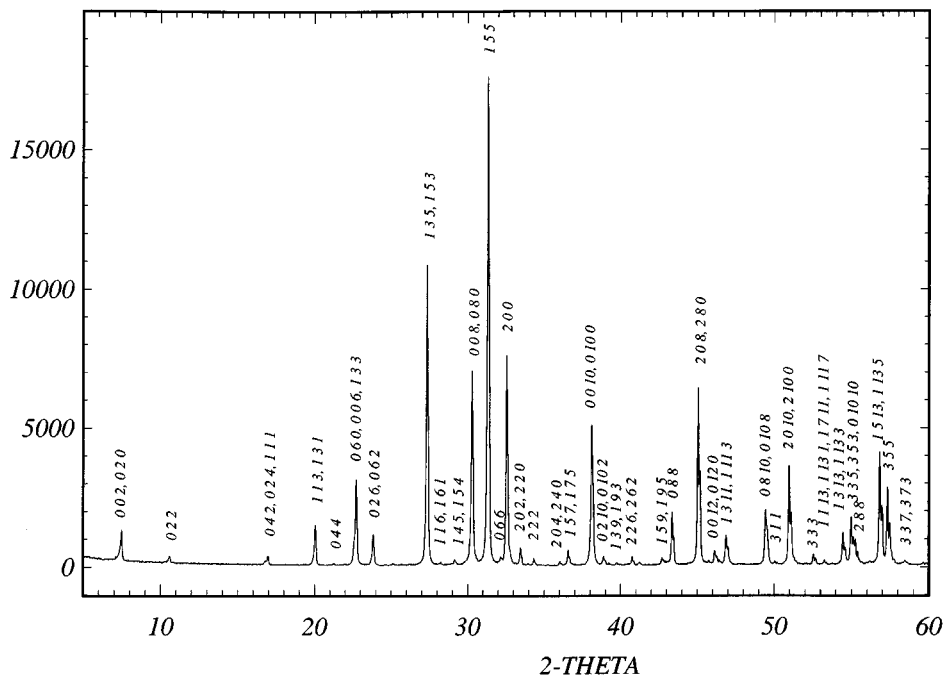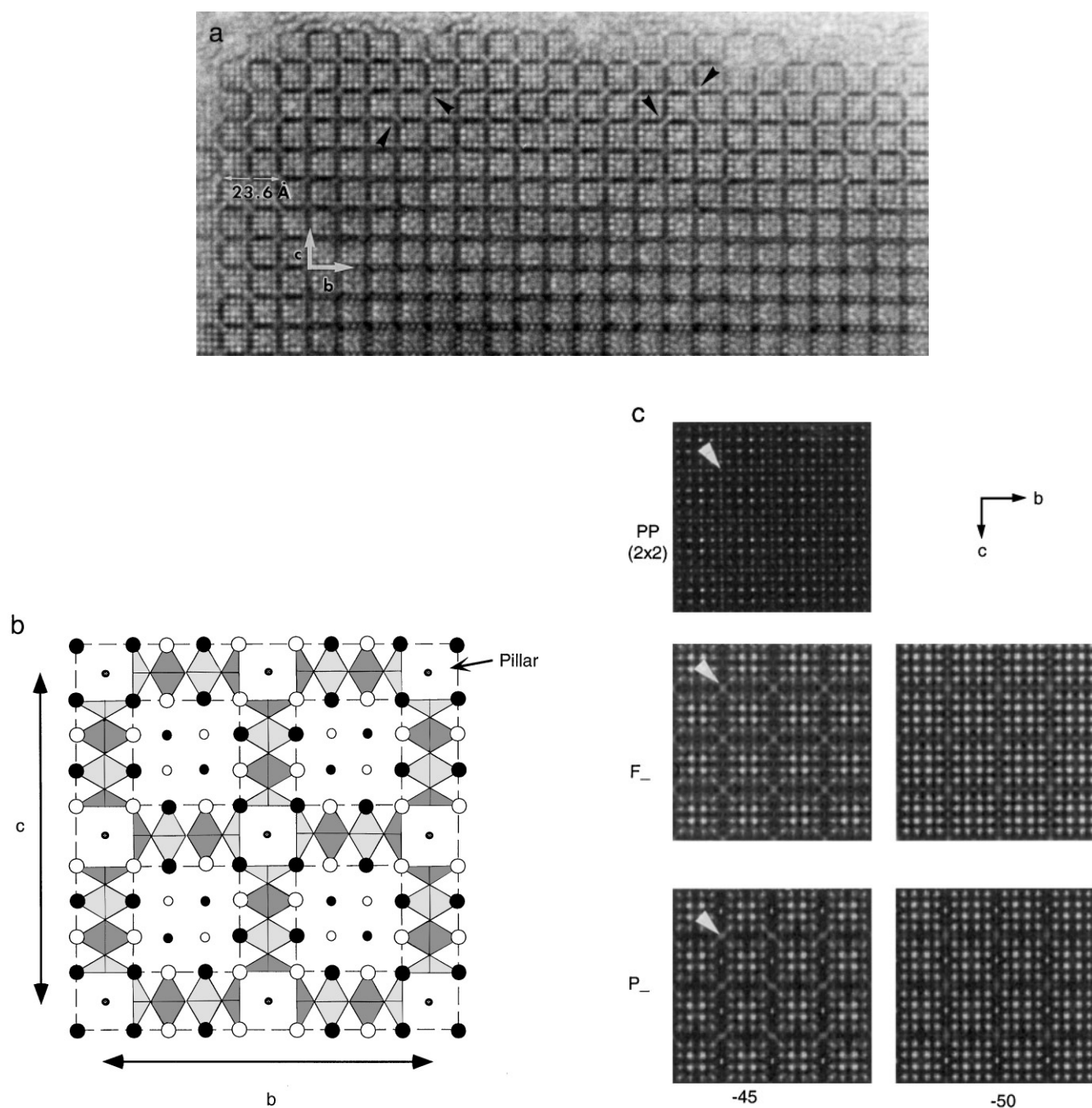A first set of positional parameters in the $Fmmm$ space group was calculated from the ideal model deduced from

FIG. 2. Powder X-ray diffraction pattern limited to $2\theta \leq 60°$ registered with CuKα radiation ($\lambda = 1.5418$ Å). The indexes refer to $Pbnb$ space group.

FIG. 3. (a) [100] HREM image. In some places, the elongated, cross-shaped contrast observed at the level of the pillar is indicated by black triangles; (b) projection of the idealized model of the "tubular-2" structure; (c) projected potential (PP 2×2 cells), and comparison between the images calculated for the F-type and P-type models (the focus values are -45 and -50 nm respectively).

the HREM study and refined from neutron data. Convergence was obtained for the refined values listed in Table 1, leading to a Bragg R factor $R_B = 0.078$. These results confirm the proposed model for this new structure, i.e., a "tubular-2" structure, and the slight bismuth deficiency, with regard to the theoretical value, deduced from EDX analysis.

Thanks to the structural particularities of the "tubular-2" structure, two ways to describe the location of the manganese atoms exist. The first is to consider that the manganese atoms are located in two types of atomic rows: one is parallel to **b** and belongs to the 2201 slice; whereas the second is parallel to **c** and belongs to the perovskite-related

TABLE 1
Refined Variable Parameters in the Space Group *Fmmm*
(Estimated Standard Deviations Refer to the Last Digit)

Atom	Site	x	y	z	B (Å^2)	n
Bi	16m	0	0.3133(3)	0.1906(4)	0.3(1)	14.2(2)
Mn1	8h	0	0.0886(9)	0	0.8(2)	8
Mn2	8h	0	0.307(1)	0	0.8(2)	8
Mn3	8i	0	0	0.0702(9)	0.8(2)	8
Mn4	8i	0	0	0.301(1)	0.8(2)	8
Sr1	16m	0	0.1984(4)	0.0758(4)	1.04(6)	16
Sr2	16m	0	0.0808(5)	0.4182(4)	1.04(6)	16
Sr3	16m	0	0.0807(5)	0.1921(4)	1.04(6)	16
O1	32p	0.119(1)	0.1806(7)	0.1906(5)	0.83(6)	15.0(3)
O2	16o	0.257(2)	0.1366(6)	0	0.83(6)	16
O3	16o	0.220(4)	0.253(2)	0	0.83(6)	8
O4	16n	0.284(2)	0	0.1336(5)	0.83(6)	16
O5	8d	0.25	0	0.25	0.83(6)	8
O6	16m	−0.037(2)	0.3118(5)	0.0973(6)	0.83(6)	16
O7	16m	0	0.0826(4)	0.0732(6)	0.83(6)	16
O8	16m	0	0.1040(5)	0.3012(5)	0.83(6)	16
O9	32p	0.25	0.0271(8)	0.014(1)	0.83(6)	8.0(3)

Space group	Cell parameters	R factors
	$a = 5.4945(1)$ Å	$R_p = 0.047$
Fmmm (n°69)	$b = 23.594(1)$ Å	$R_{wp} = 0.062$
	$c = 23.581(1)$ Å	$R_B = 0.076$

slice. The second way is to consider that the manganese atoms belong to equivalent but perpendicular "octahedral" layers of the 2201 structure. Both are sandwiched between two [SrO] rows, and the crossing of the two manganese rows forms "pillars' characterized by the existence of square Mn_4 "cycles" of four edge-sharing manganese polyhedra (the four Mn atoms are located at the same x). In the tubular-4 cuprate, the "pillars" were shown to be only partially occupied by oxygen atoms (12), so that the copper atoms belonging to the cycle form either CuO_5 bipyramids (for the occupied oxygen position in the pillar) or CuO_4 tetrahedra (for the vacant position). But a higher occupancy of these oxygen sites is possible and has to be taken into consideration, especially in the case of manganese, which tends to form MnO_6 octahedra. The neutron diffraction study confirms this viewpoint. It shows the presence of extra oxygen, labeled O(9) in Table 1, inside the pillar so that the ideal formula of the perovskite slice is no longer $[Sr_8Mn_6O_{16}]_\infty$ but rather $[Sr_8Mn_6O_{16+\delta}]_\infty$. The refined oxygen content (eight per unit cell) is higher than that observed in the copper-based "tubular-4" compound (4.3 per unit cell (12)). These oxygen atoms are randomly distributed over the positions of the (32p) crystallographic site (x, y, z with $x = 0.25$, $y = 0.011$, and $z = 0.028$), but this implies that two oxygens are present in a pillar, one at $x = 0.25$ and the second at $x = 0.75$, to avoid oxygen–oxygen distances that are too short. For a given x value, oxygen

occupies one of the four positions generated by the space group. This situation is different from that observed for the copper-based "tubular-4" structure and involves Mn–O polyhedra different than the Cu–O ones for the atoms forming the "cycle." Seeking additional information about the pillar, particular attention was paid to the HREM images. The theoretical HREM images, calculated from the refined positional parameters given in Table 1, showed that two of the characteristic contrasts of the "pillar" are one very bright spot (correlated to a light electron density zone) and a cross-shaped bright dot. In every case, whatever the focus value, a fourfold symmetry is calculated for the positional parameters of the average structure (F-type lattice). An example is given in Fig. 3c (labeled F_) for focus values of −45 and −50 nm, which are assumed to be close to the experimental values in Fig. 3a. In fact, a contrast anomaly in the thin edges of the crystallites is detected at this level. For a few focus values, the contrast is not symmetrical but consists in one elongated dot, extended along one of the pillar diagonals (see for example the black triangles in Fig. 3a). The orientation of these elongated dots varies from one pillar to the adjacent ones, so that artifact effects such as small crystal or beam tilting, which were shown to be crucial for tunnel structures, can be discarded. This suggests that, in the oxygen rows running along **a** within the pillars, the distribution of the oxygen atoms is not really statistical over the four positions generated by the F-type lattice. The space group *Pbnb*, determined by considering the weak extra reflections in the ED patterns, allows the initial (32p) site of the oxygen O(9) to be divided into independent (8e) crystallographic sites.

Actual Structure

Working in the *Pbnb* space group implies an increase in the number of independent atoms relative to the *Fmmm* space group. Positional parameters issued from the average structure (Table 1) were calculated to be compatible with *Pbnb* and used as starting parameters. Particular attention was paid to the oxygen atoms located inside the pillar. Considering an oxygen-free pillar, the Fourier difference map section calculated at $x = 0.25$ clearly showed two residues approximately symmetrical with regard to the origin, with coordinates $y \approx z \approx 0.015$ (Fig. 4). Two sets of oxygen labeled O(16) and O′(16) and located in the (8e) crystallographic site with half occupancy were then introduced in the calculations. Refinements of positional parameters, bismuth occupancy, and isotropic B factors for each kind of atoms allowed the following R factors to be obtained: $R_p = 0.039$, $R_{wp} = 0.051$, and $R_B = 0.063$. Note that these values are significantly lower than those obtained using the *Fmmm* space group (Table 1). Finally, occupancies of all oxygen sites were refined, leading to a decrease of R factors: $R_p = 0.037$, $R_{wp} = 0.048$, and $R_B = 0.057$. Note that it was
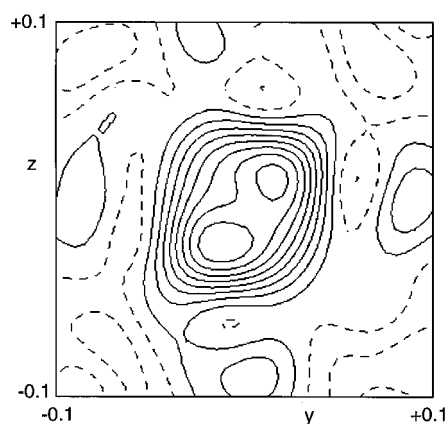
FIG. 4. Fourier difference map section at $x = 0.25$ calculated in the space group *Pbnb* and showing the two residues attributed to the oxygens (O(16) and O′(16)) located inside the pillar.

not possible to show any difference between the occupancy of O(16) and O′(16) sites. The refined values are listed in Table 2 and the corresponding calculated diffraction pattern is drawn in Fig. 5. Based on the R values, the results can be considered to be representative of the structure.

As indicated above, the use of *Pbnb* space group increases the number of independent atoms compared to the F-type space groups. Most of them, except manganese and some oxygen atoms, are multiplied by a factor of two. Constraints on the coordinates would permit a pseudo-F lattice: for example, for bismuth one should have $y_{Bi(2)} = 1 - y_{Bi(1)}$ and $z_{Bi(2)} = z_{Bi(1)}$. The examination of Table 2 shows that, even if the above relations are not verified, the displacements which violate these conditions remain small. This point will be discussed further.

It is interesting to compare the Bi–O plane (Fig. 6a) with that observed in the "tubular 4" phase $Bi_4Sr_8Cu_5O_{19+y}$ (11, 12) (Fig. 6b). The Bi–O plane of the "tubular-2" phase can be described as the analogous plane in the "tubular-4" phase with the zigzagging Bi–O chain characteristic of the bismuth-based layered cuprates removed. The bismuth environment is similar to that of bismuth located at the border of the Bi–O plane in the copper-based phase, i.e., three approximately perpendicular Bi–O bonds considering only the short distances listed in Table 3. Among them, one distance (1.85 Å) is very short compared to the others and smaller than those usually reported. However, Bi–O distances as short as 1.74, 1.80, and 1.88 Å, have already been reported in $Bi_{18}Ni_8O_{36}$ (15), $Bi_2Sr_2Fe_2O_{9.2}$ (16), and $Bi_2Sr_2MnO_{6.25}$ (16), respectively.

The strontium–oxygen distances, which range between 2.39 and 2.98 Å, are comparable with those usually encountered in layered cuprates.

Manganese atoms, which do not participate to the pillar (Mn(2) and Mn(4)), are surrounded by six oxygen atoms

TABLE 2
**Refined Variable Parameters in the *Pbnb* Space Group (Estimated Standard Deviations Refer to the Last Digit)**

Atom	Site	x	y	z	$B(\text{Å}^2)$	n
Bi(1)	8e	0	0.3081(7)	0.1910(7)	$0.4(1)^a$	8^f
Bi(2)	8e	0	0.6866(8)	0.1879(9)	$0.4(1)^a$	6.1(1)
Mn(1)	8e	0	0.0866(9)	0	$0.8(1)^b$	8^f
Mn(2)	8e	0	0.3101(9)	0	$0.8(1)^b$	8^f
Mn(3)	8e	0	0	0.0747(9)	$0.8(1)^b$	8^f
Mn(4)	8e	0	0	0.3038(9)	$0.8(1)^b$	8^f
Sr(1)	8e	0	0.1976(7)	0.0762(9)	$0.7(3)^c$	8^f
Sr(2)	8e	0	0.8005(7)	0.0754(8)	$0.7(3)^c$	8^f
Sr(3)	8e	0	0.0844(7)	0.4149(8)	$0.7(3)^c$	8^f
Sr(4)	8e	0	0.9282(7)	0.4180(9)	$0.7(3)^c$	8^f
Sr(5)	8e	0	0.0854(7)	0.1909(6)	$0.7(3)^c$	8^f
Sr(6)	8e	0	0.9237(6)	0.1909(8)	$0.7(3)^c$	8^f
O(1)	8e	0.124(3)	0.182(1)	0.192(1)	$1.02(5)^d$	8^f
O(2)	8e	0.091(3)	0.816(1)	0.176(1)	$1.02(5)^d$	7.2(4)
O(3)	8e	0.283(5)	0.132(1)	0	$1.02(5)^d$	8^f
O(4)	8e	0.740(4)	0.139(1)	0	$1.02(5)^d$	8^f
O(5)	8e	0.219(3)	0.249(1)	0	$1.02(5)^d$	7.2(2)
O(6)	8e	0.271(4)	0	0.136(1)	$1.02(5)^d$	8^f
O(7)	8e	0.722(4)	0	0.135(1)	$1.02(5)^d$	8^f
O(8)	4d	0.75	0	0.25	$1.02(5)^d$	4^f
O(9)	4c	0.25	0	0.25	$1.02(5)^d$	4^f
O(10)	8e	−0.012(5)	0.3084(9)	0.0948(8)	$1.02(5)^d$	8^f
O(11)	8e	0	0.6963(8)	0.0943(9)	$1.02(5)^d$	8^f
O(12)	8e	0	0.0898(7)	0.0816(8)	$1.02(5)^d$	7.3(2)
O(13)	8e	−0.012(5)	0.9238(7)	0.0728(8)	$1.02(5)^d$	8^f
O(14)	8e	0	0.1087(8)	0.3047(9)	$1.02(5)^d$	8^f
O(15)	8e	0.029(5)	0.8959(9)	0.3108(8)	$1.02(5)^d$	5.9(3)
O(16)	8e	0.25	$0.0248(7)^e$	$0.0130(9)^e$	$1.02(5)^d$	4^f
O′(16)	8e	0.25	$-0.0248(7)^e$	$-0.0130(9)^e$	$1.02(5)^d$	4^f

Space group	Cell parameters	R factors
	$a = 5.4946(1)$ Å	$R_p = 0.037$
Pbnb (n°56)	$b = 23.595(1)$ Å	$R_{wp} = 0.048$
	$c = 23.580(1)$ Å	$R_B = 0.057$

^{a,b,c,d}Parameters constrained at the same value.
^{e}Constrain $x' = -x$, $y' = -y$.
^{f}Full occupancy considered since value of ESD is greater than the shifting.

forming distorted octahedra characterized by four unequal, short equatorial Mn–O distances and two apical long distances. Along **b**, one Mn(2) octahedron shares its corners with two other Mn(2) octahedra on one side and two Mn(1) polyhedra on the other side. The same sequence is observed along **c** for Mn(4) octahedra and Mn(3) polyhedra (Fig. 7). The nature of the Mn(1) and Mn(3) polyhedra forming the pillars is more complex due to the presence of oxygens O(16) and O′(16); they cannot coexist with the same x value because the O–O distance would be too short (close to 1.3 Å). This implies that the site occupancies cannot exceed 50%; i.e., two oxygens per pillar or eight oxygens per unit cell. Two possibilities occur depending on the position of oxygen atoms inside the pillar. If the pillar is occupied by
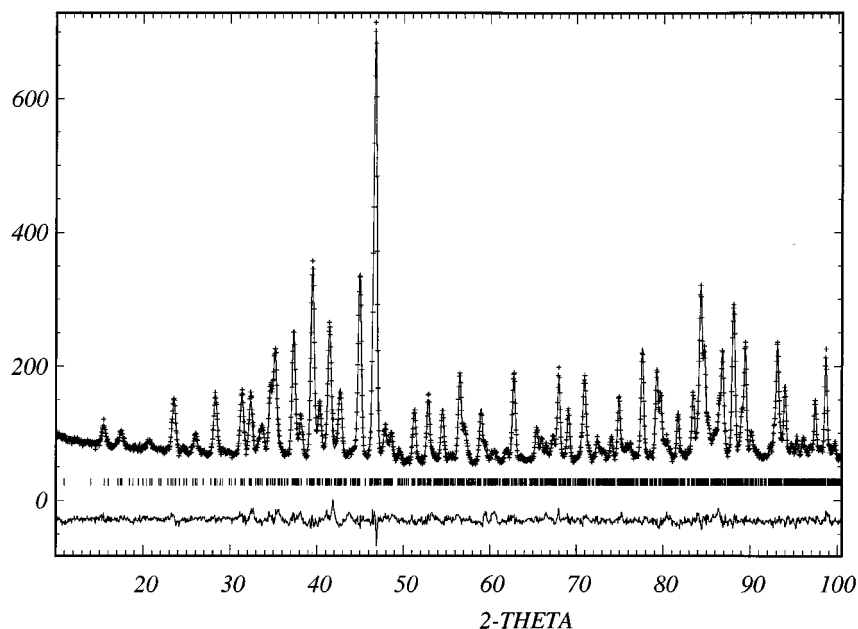
FIG. 5. Powder neutron diffraction patterns ($\lambda = 1.5938$ Å) limited to $2\theta \leq 100°$; crosses refer to the experimental pattern, whereas the calculated and difference patterns are drawn with hatched and solid lines respectively. The vertical bars indicate the Bragg angle positions.

one O(16) and one O'(16), for the reason given above, they necessarily have the same y and z values and differ only by x (0.25 and 0.75). In this configuration, the pillar can be described as built up from two edge-sharing distorted $Mn(3)O_6$ octahedra which share a face with a distorted $Mn(1)O_6$ octahedron on one side and one corner with a $Mn(1)O_4$ tetrahedron on the other side (Fig. 8a). If the pillar is occupied by two oxygens O(16) (or two O'(16)), it can be described as built up from two edge-sharing distorted $Mn(3)O_6$ octahedra and $Mn(1)O_5$ pyramids (Fig. 8b). The

latter model seems more likely than the former, which generates two different $Mn(1)O_n$ polyhedra and a particularly unusual connection (one common face) between two octahedra. So, from the second configuration, we can calculate for each MnO_n polyhedron an average Mn–O distance ($\bar{d}$) from which the manganese atoms can be listed in two groups: Mn(1) and Mn(2) with short ($\bar{d}$) values (1.91 and 2.00 Å, respectively); and Mn(3) and Mn(4) with longer ($\bar{d}$) values (2.12 and 2.09 Å, respectively). These values are close to those usually observed for Mn^{3+} in oxides (1.90–1.95 Å
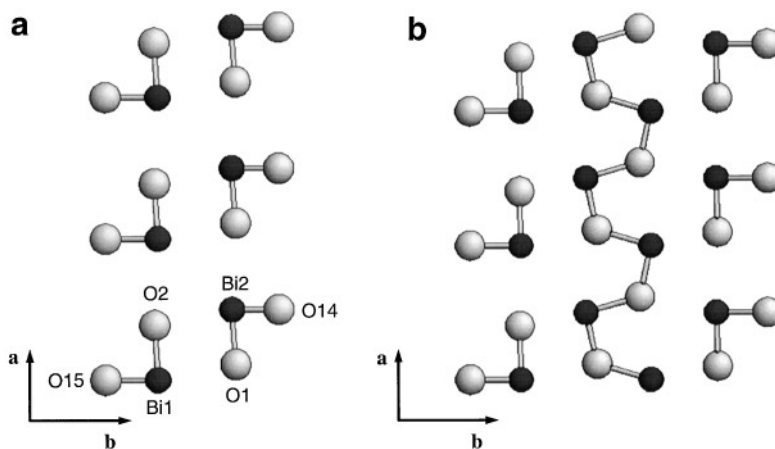
FIG. 6. Drawing of the bismuth-oxygen plane in (a) the "tubular-2" phase and (b) the "tubular-4" phase.

TABLE 3
Interatomic Metal–Oxygen Distances (Å)

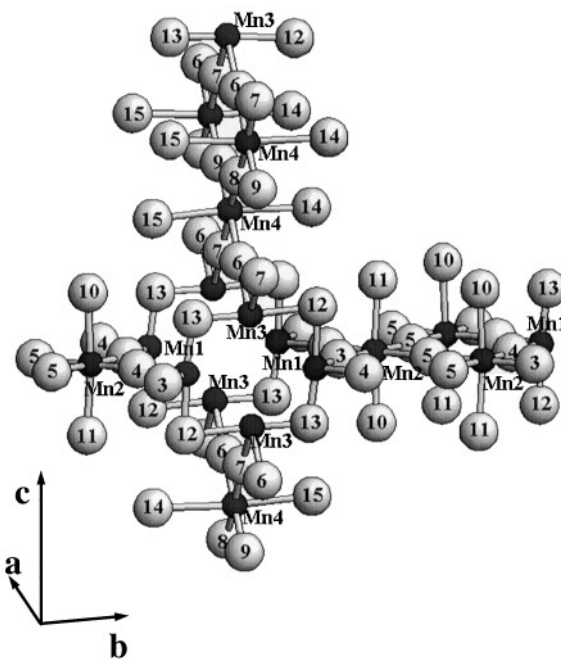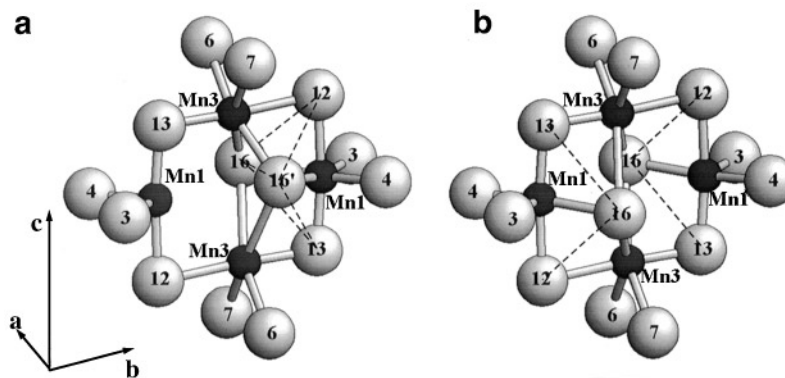|					
Bi–O distances					
Bi(1)–O(2)	×1	2.28(2)	Bi(2)–O(1)	×1	2.07(2)
Bi(1)–O(10)	×1	2.27(2)	Bi(2)–O(1)	×1	2.91(3)
Bi(1)–O(15)	×1	2.08(2)	Bi(2)–O(11)	×1	2.22(2)
			Bi(2)–O(14)	×1	1.85(2)
Sr–O distances					
Sr(1)–O(1)	×1	2.84(3)	Sr(4)–O(3)	×1	2.67(2)
Sr(1)–O(3)	×1	2.84(2)	Sr(4)–O(4)	×1	2.83(2)
Sr(1)–O(4)	×1	2.68(2)	Sr(4)–O(6)	×1	2.46(2)
Sr(1)–O(5)	×1	2.48(2)	Sr(4)–O(7)	×1	2.44(2)
Sr(1)–O(5)	×1	2.68(2)	Sr(4)–O(10)	×1	2.84(2)
Sr(1)–O(10)	×1	2.65(3)	Sr(4)–O(13)	×1	2.69(3)
Sr(1)–O(11)	×2	2.781(4)	Sr(4)–O(13)	×1	2.82(3)
Sr(1)–O(12)	×1	2.55(2)	Sr(4)–O(15)	×1	2.65(3)
			Sr(4)–O(16)	×1	2.85(2)
Sr(2)–O(2)	×1	2.45(2)	Sr(4)–O'(16)	×1	2.85(2)
Sr(2)–O(3)	×1	2.85(2)			
Sr(2)–O(4)	×1	2.69(2)	Sr(5)–O(1)	×1	2.39(2)
Sr(2)–O(5)	×1	2.65(2)	Sr(5)–O(6)	×1	2.82(2)
Sr(2)–O(5)	×1	2.44(2)	Sr(5)–O(7)	×1	2.85(2)
Sr(2)–O(10)	×1	2.72(3)	Sr(5)–O(8)	×1	2.809(2)
Sr(2)–O(10)	×1	2.86(3)	Sr(5)–O(9)	×1	2.809(2)
Sr(2)–O(11)	×1	2.50(2)	Sr(5)–O(12)	×1	2.58(2)
Sr(2)–O(13)	×1	2.91(2)	Sr(5)–O(14)	×1	2.74(2)
			Sr(5)–O(14)	×2	2.804(5)
Sr(3)–O(3)	×1	2.59(2)			
Sr(3)–O(4)	×1	2.73(2)	Sr(6)–O(2)	×1	2.62(3)
Sr(3)–O(6)	×1	2.64(2)	Sr(6)–O(6)	×1	2.67(2)
Sr(3)–O(7)	×1	2.62(2)	Sr(6)–O(7)	×1	2.70(2)
Sr(3)–O(11)	×1	2.65(2)	Sr(6)–O(8)	×1	2.658(2)
Sr(3)–O(12)	×2	2.752(3)	Sr(6)–O(9)	×1	2.658(2)
Sr(3)–O(14)	×1	2.66(3)	Sr(6)–O(13)	×2	2.78(2)
Sr(3)–O(16)	×1	2.60(2)	Sr(6)–O(15)	×1	2.91(3)
Sr(3)–O'(16)	×1	2.60(2)	Sr(6)–O(15)	×1	2.98(3)
			Sr(6)–O(15)	×1	2.67(3)
Mn–O distances					
Mn(1)–O(3)	×1	1.88(2)	Mn(3)–O(6)	×1	2.07(3)
Mn(1)–O(4)	×1	1.89(2)	Mn(3)–O(7)	×1	2.09(3)
Mn(1)–O(12)	×1	1.93(2)	Mn(3)–O(12)	×1	2.13(2)
Mn(1)–O(13)	×1	1.74(2)	Mn(3)–O(13)	×1	2.80(2)
Mn(1)–O(16)	×1	2.02(2)	Mn(3)–O(16)	×1	2.08(2)
Mn(1)–O(16)	×1	2.98(2)	Mn(3)–O(16)	×1	2.55(2)
Mn(1)–O'(16)	×1	2.98(2)	Mn(3)–O'(16)	×1	2.55(2)
Mn(1)–O'(16)	×1	2.02(2)	Mn(3)–O'(16)	×1	2.08(2)
Mn(2)–O(3)	×1	1.82(3)	Mn(4)–O(6)	×1	1.90(3)
Mn(2)–O(4)	×1	1.78(3)	Mn(4)–O(7)	×1	1.88(3)
Mn(2)–O(5)	×1	1.88(3)	Mn(4)–O(8)	×1	1.87(2)
Mn(2)–O(5)	×1	2.08(2)	Mn(4)–O(9)	×1	1.87(2)
Mn(2)–O(10)	×1	2.24(2)	Mn(4)–O(14)	×1	2.56(2)
Mn(2)–O(11)	×1	2.23(2)	Mn(4)–O(15)	×1	2.47(2)

FIG. 7. Perspective view of a part of the manganese-oxygen framework. The atoms are labeled. For simplicity the oxygens inside the pillar are not drawn.

Mn^{3+} in this compound agrees with the mean oxidation state deduced from the oxygen stoichiometry refinements (Table 2), which lead to $Mn^{2.89+}$, assuming trivalent bismuth.

These calculations using the atomic positions of the *Pbnb* space group allow two structural features related to the positions of the Bi atoms and the oxygen atoms in the pillar to be highlighted. Each of these points is discussed considering neutron analysis and HREM information.

(*i*) *Lattice distortion.* [010] images clearly reveal the lowering of the symmetry from the average F-type to the actual P-type lattices (Fig. 9). Along [010], the experimental contrast is very similar to that observed for the $Bi_2Sr_2MnO_6$ oxides, although the composition of the atom columns is considerably more complex. For a focus value close to -55 nm, the contrast consists of two rows of bright spots, correlated to the projected positions of 2Bi, 2Sr and 1Mn atoms. They are sandwiched between two other rows of bright spots, correlated to the projected positions of 4Sr and 1Mn. These groups of four rows are separated by one single row of small gray dots, which correspond to the Mn positions. Theoretically, according to the F-type lattice, these images would provide a periodicity of 2.7 Å along **b**. In fact, a contrast modulation is observed locally at the level of the "double Bi" rows consisting of one bright dot alternating with one gray dot; this alternation is shifted by 2.7 Å in the adjacent double row (this arrangement is outlined by

for manganese in pyramidal coordination, 2.00 Å or greater for Mn in octahedral coordination). Note that the mean Mn(1)–O distance is close to that observed for MnO_5 pyramids and supports the second model. The presence of

FIG. 8. Perspective view of the structure of the pillar. (a) If one O(16) and O'(16)) are present, it results in two edge-sharing Mn(3)O$_6$ octahedra having one face and one corner in common with a Mn(1)O$_6$ octahedron and a Mn(1)O$_4$ tetrahedron respectively (the common faces are outlined with dotted lines). (b) In the case of two O(16) (or two O'(16)), the pillar is built with two edge-sharing Mn(3)O$_6$ octahedra and two Mn(1)O$_5$ pyramids (the common edges are outlined with dotted lines).

dark circles in Fig. 9). This doubling of the periodicity along **b** is in agreement with the small bismuth displacements observed in the *Pbnb* space group with regard to the theoretical and ideal positions of the F-type structure. This modulation is clearly observed in the calculated images. A similar variation of contrast was reported by several authors for the Bi cuprates (18) and manganites (19), and correlated to the effect of the displacive modulation of the Bi atoms. In the present structure, the incommensurate modulation does not exist but is replaced by the periodic variation in the nature of the layers stacked along that direction, due to the presence of the perovskite-related slice.

Note that this modulation is not observed over whole crystals but only in the form of domains. This observation is consistent with the superposition of the [010] and [001] variants, as systematically observed form ED patterns (Fig. 1).

(*ii*) *Structure of the pillar.* The second point deals with the problem of the oxygen located in the pillar and the manganese polyhedra forming the cycle. In the average
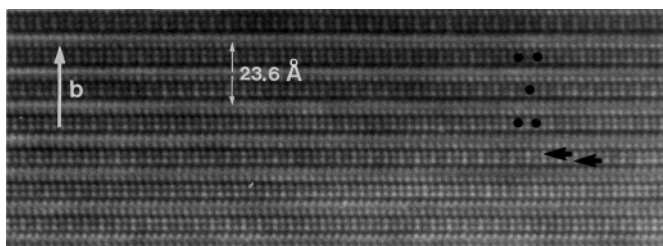

FIG. 9. [010] HREM image showing the contrast modulation at the level of the double (Bi, SrO) layers, correlated to the lowering of symmetry. The alternation of bright and less bright dots along **b** is indicated by black arrows, and the translation in the adjacent double layers is outlined by black full circles.

structure, i.e., the F-type lattice, there is a single position for this oxygen, while in the *Pbnb* space group, two independent positions are available. For the HREM image calculations, one site of the oxygen in the pillar out of two was considered fully occupied and the second vacant see Fig. 8b), in agreement with the above structural discussion. The theoretical images (labeled P_- in Fig. 3c) simulated for this model show that a contrast similar to that experimentally recorded is generated at the level of the pillar, i.e., the formation of elongated bright dots, extended along the diagonal of the "pillar". The images calculated for focus values close to -45 and -50 nm are compared directly with the equivalent values for the *Fmmm* model (labeled F_- in Fig. 3c). However, a difference remains between these calculated images and the experimental images: the arrangement of the elongated spots is perfectly ordered in the calculated images, alternately elongated along [011] and [0$\bar{1}$1], as a direct consequence of the translations imposed by the space group *Pbnb*, whereas they are often randomly distributed in the experimental images. This point can be easily understood, assuming that the oxygen site is partly occupied. The random occupation, i.e., the superposition along **a** of the possible orientations of the double octahedra blocks and the existence of twinning domains implies that the effect of contrast asymmetry is no longer observed at the level of the pillar as soon as the crystal thickness increases.

Defective Structure

Most of the crystallites exhibit regular layer stacking; only a few defects, such as the intercalation of extra layers or shifting mechanisms, were detected.

The first type of defect corresponds to the formation of $n = 4$ members (Fig. 10a). Locally, the perovskite-related
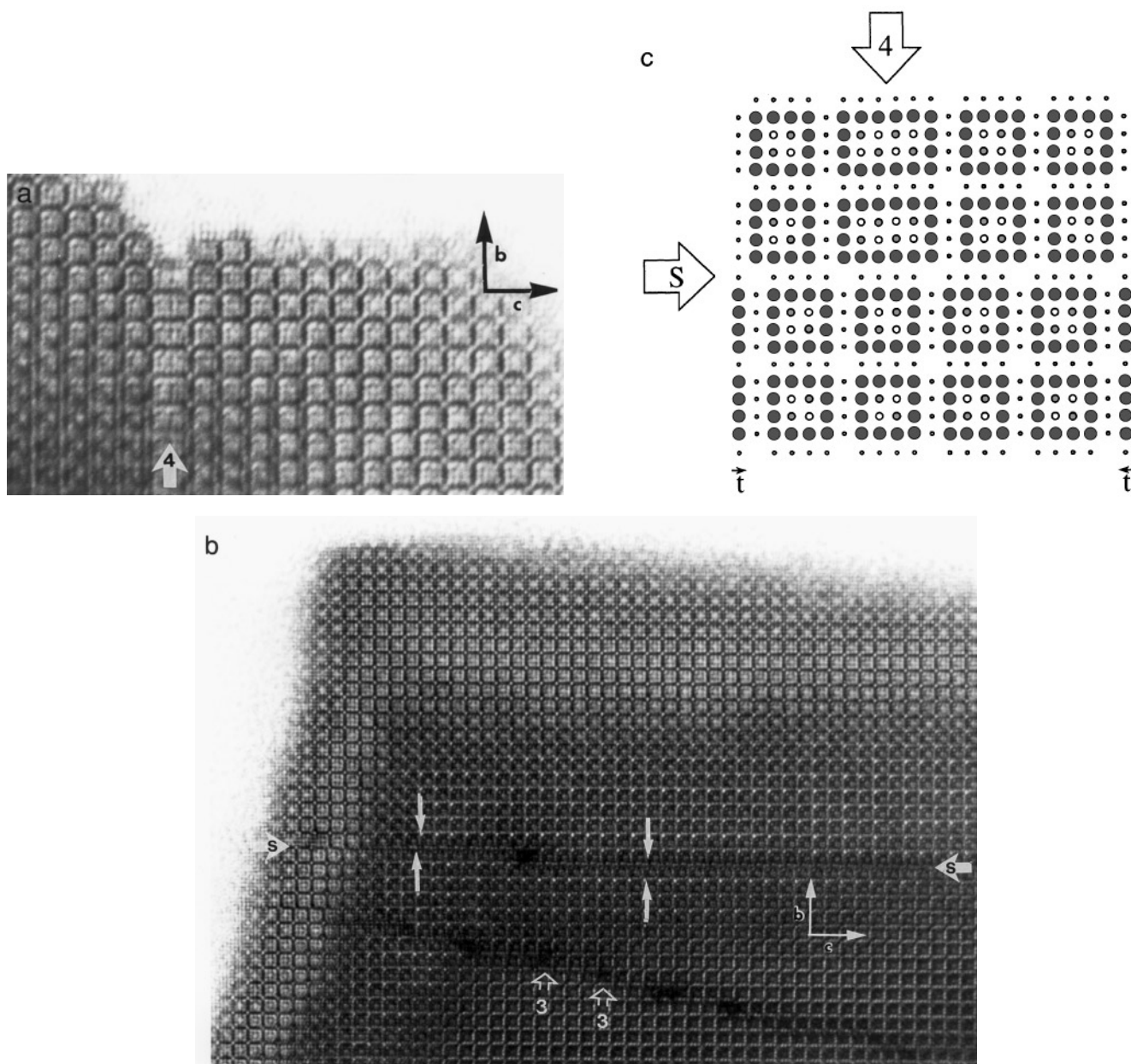
FIG. 10. [100] HREM images of defective areas: (a) example of $n = 4$ member; (b) formation of shearing plane (the possible translation of this defect along **c** is shown by white arrows); (c) idealized drawing of the two types of defects projected onto (100) plane. For simplicity only cations are drawn. Bismuth atoms are schematized by medium circles whose the color depends on the x value (0 or 1/2).

slices [Sr$_8$Mn$_6$O$_{16+\delta}$]$_\infty$ are separated by four (010) [Bi$_2$Sr$_2$MnO$_6$]$_\infty$ slices; defective members are indicated in the images by white arrows labeled 4, and the idealized drawing is given in Fig. 10c. In some places, adjacent defective $n = 4$ members are observed (see white arrow "4-4" in Fig. 11); this can be considered a favorable sign for the stabilization of the $n = 4$ member. Another interesting point is that the defects occur along two perpendicular directions (see white arrow labelled "4⊥" in Fig 11). The fact that defective members arise equally along **b** and **c** emphasizes

the pseudotetragonal character of the $n = 2$ "tubular" structure, in contrast with the higher-n members (of the cuprates), where defects only arise, of course, along **b**.

The second type of defect indicated by white arrows labeled "S" in Fig. 10b) results from a shifting of the structure at the level of the manganese layers. The amplitude of the translation is about $a_p\sqrt{2}/2$. As a result, the manganese layers perpendicular to the direction of translation are no longer facing but connected to one (010) [Sr$_4$MnO$_6$]$_\infty$ layer. One (010) [Bi$_2$Sr$_2$MnO$_6$]$_\infty$ layer out of two is connected to

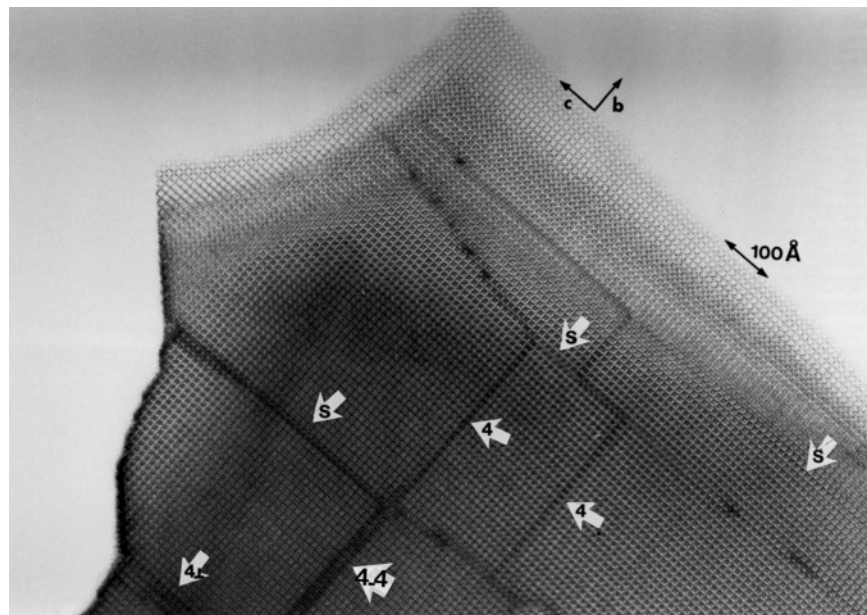**FIG. 11.** Overall [100] image of a crystallite exhibiting a high density of defects.

another (010) $[Bi_2Sr_2MnO_6]_\infty$ layer, whereas the second is connected to one $[Sr_4MnO_6]_\infty$ layer (a schematic drawing is given in Fig. 10c). Similar defects were previously reported in the "tubular" cuprates (13, 20, 21) and were also observed to be formed periodically in the so-called "monoclinic tubular" phases for the $n = 7$ member (21) and the Li-doped cuprates (22). In such a defect, the pillars are destroyed because the manganese layers no longer cross over a single point. In this "tubular-2" manganite, shearing planes are also observed along two perpendicular **b** and **c** directions.

The intergrowth and shearing mechanisms are formed without any strong distortion of the structure. This can be observed in the overall image (Fig. 11) of a rare crystallite which exhibits a particularly, high density of defects. Moreover, it can be observed that the (010) or (001) shearing planes are easily translated along one of the perpendicular directions (compare the levels of the long white arrows, which are at the level of the manganese layers on both sides of the shearing plane in Fig. 10b) or even propagated along inclined directions as the result of successive translations (Fig. 11).

The two types of defects, higher n members and shearing planes, are often coupled, facilitating their accommodation by the framework. As an example, a $n = 4$ member formed perpendicular to a shearing plane is drawn in Fig. 10c. The width difference between the $n = 4$ member and the $n = 2$ regular matrix is accommodated by the fact that the translation vectors (correlated to the shearing mechanisms) are in opposite directions in the two parts of the matrix separated by the defective $n = 4$ member.

A last remark deals with the fact that $n = 3$ members can be formed at the level of the translation of the shearing plane (see open white arrows labeled 3 in Fig. 10b), whereas they were never observed in the form of "stabilized" defective slices. This behavior is similar to that observed in the cuprates, where the $n < 4$ members were not observed, except in defective areas where the shearing mechanism is translated (13).

TRANSPORT AND MAGNETIC PROPERTIES

This new phase is an insulator characterized by a very high resistivity even at room temperature ($\rho_{300K} > 10^6$ Ω/cm). In order to get more information concerning its physical properties, magnetic susceptibility $\chi(T)$ measurements (Faraday method) in 3 kG were also performed. In Fig. 12, the $\chi(T)$ curve in the range 100–800 K (labeled a) is reported, while $\chi^{-1}(T)$ values up to 400 K are plotted in the inset, with the solid line corresponding to a fit from a Curie-Weiss law:

$$\chi = \chi_0 + C/(T - \theta p).$$

The effective moment per manganese deduced from this fit, $\mu_{eff} = 4.7$ μ_B, is close to that expected for high-spin Mn^{3+} ($\mu_{theoritical} = 4.9$ μ_B). This value is consistent with the valence state of manganese ($+2.89$) inferred from the chemical formula deduced from neutron data refinements. Moreover this fitting also leads to a negative θp value, $\theta p = -650$ K, characteristic of dominant antiferromagnetic interactions between magnetic Mn^{3+} species. A comparative study performed on the parent 2201 structure $Bi_2Sr_2MnO_{6+\delta}$, synthesized in the same experimental conditions as the $n = 2$ tubular, shows that the χ values for this new manganite are deeply depressed. The peak observed on the $\chi(T)$ curve (labeled b in Fig. 12) of the 2201 phase is in agreement with
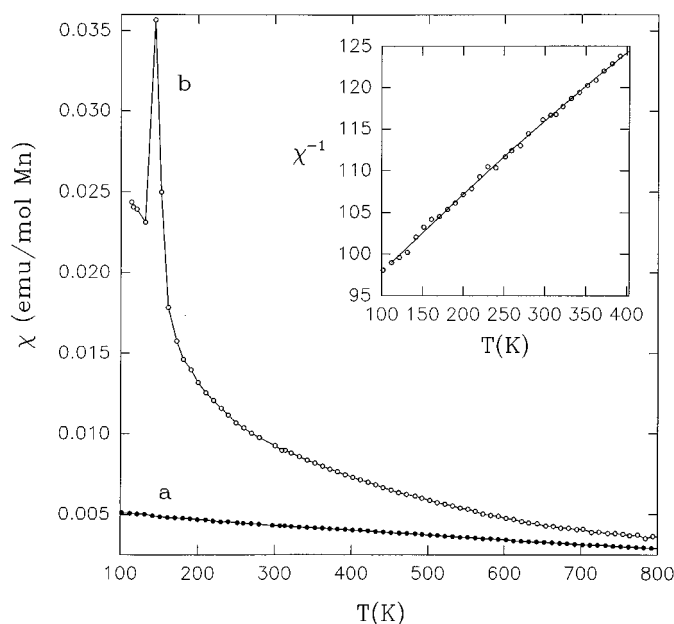
FIG. 12. Molar susceptibility magnetic $\chi(T)$ registered in 3 kG for a) Bi$_4$Sr$_{12}$Mn$_8$O$_{28+\delta}$ and b) Bi$_2$Sr$_2$MnO$_{6+\delta}$. The inset shows the $\chi^{-1}(T)$ values between 100 and 400 K and the corresponding data to the fitting from Curie-Weiss law (solid line).

previously reported data (7) and was correlated to ferro-magnetic behavior. The strong decrease of the χ values in the case of the $n = 2$ tubular phase suggests that long-range magnetic order cannot develop. This feature is not surpris-ing if one considers that this tubular structure exhibits several kinds of MnO$_n$ polyhedra at the level of pillars. The overlaping Mn–O orbitals are thus periodically modified, leading to the localization of the charge carriers. Accord-ingly the long-range ordering of the manganese magnetic moment is broken. The result is an insulating compound exhibiting weak antiferromagnetism.

CONCLUDING REMARKS

This study shows the ability of manganese oxides to form "tubular" structures, reinforcing the structural analogy be-tween manganese and copper oxides. Nevertheless this man-ganite differs from the previously isolated cuprates in the fact that the "Mn$_4$" pillars formed by the criss-crossing layers of manganese contain more oxygen. In other words, both series of oxides can be described as the intergrowth of "2201" type slices [Bi$_2$Sr$_2$MO$_6$]$_n$ with [Sr$_8$M$_6$O$_{16+\delta}$]-defi-cient, perovskite-related slices (M = Cu, Mn).

An interesting feature deals with the fact that this $n = 2$ member stabilized for manganese has not been observed for copper. But most interesting is the fact that it is the only member of the series that exhibits "2201" types slices oriented at 90°, i.e., parallel to (010) and (001), in agreement with its pseudotetragonal symmetry.

The extended defects observed by HREM, although rare, are of great interest. They suggest that new members in this series, as well as other original structures, may be syn-thesized by applying shearing mechanisms.

REFERENCES

1. J. G. Bednorz and K. A. Müller, *Z. Phys. B* **64,** 189 (1986).
2. See for example R. Von Helmolt, J. Wecker, B. Holzapfel, L. Schultz, and K. Sanwer, *Phys. Rev. Lett.* **71,** 2331 (1993).
3. C. Michel, M. Hervieu, M. M. Borel, F. Deslandes, J. Provost, and B. Raveau, *Z. Phys. B* **68,** 421 (1987).
4. M. Maeda, Y. Tanaka, M. Fukutomi, and T. Asano, *Jpn. J. Appl. Phys.* **L27,** 209 (1988).
5. M. A. Subramanian, C. C. Torardi, J. C. Calabrese, J. Gopalakrishnan, K. J. Morrissey, T. R. Askew, R. B. Flippen, U. Chowdhry, and A. W. Sleight, *Science* **2398,** 1015 (1988).
6. J. M. Tarascon, Y. Le Page, P. Barboux, B. G. Bagley, L. H. Greene, W. R. McKinnon, G. W. Hull, M. Giroud, and D. M. Hwang, *Phys. Rev. B* **37,** 9382 (1988).
7. W. R. McKinnon, E. Tselepsis, Y. Le Page, S. P. McAlister, G. Pleizier, J. M. Tarascon, P. F. Miceli, R. Ramesh, G. W. Hull, J. V. Waszczak, J. J. Rhyne, and D. A. Neumann, *Phys. Rev. B* **41,** 4489 (1990).
8. R. S. Roth, C. J. Rawn, and I. A. Bendersky. *J. Mater. Res.* **5,** 46 (1990).
9. Z. Hiroi, Y. Ikeda, M. Takano, and Y. Bando, *J. Mater. Res.* **6,** 435 (1991).
10. M. Hervieu, C. Michel, A. Q. Pham, and B. Raveau, *J Solid State Chem.* **104,** 338 (1993).
11. A. Fuertes, C. Miratvilles, J. Gonzalez-Calbet, M. Vallet-Regi, X. Obradors, and J. Rodriguez-Carvajal, *Physica C* **157,** 529 (1989).
12. M. T. Caldes, J. M. Navarro, F. Perez, M. Canera, J. Fontuberta, M. Casan-Pastor, C. Miratvilles, X. Obradors, J. Rodriguez-Carvajal, J. M. Gonzalez-Calbet, M. Vallet-Regi, A. Garcia, and A. Fuertes, *Chem. Mater.* **3,** 844 (1991).
13. M. T. Caldes, M. Hervieu, A. Fuertes, and B. Raveau, *J. Solid State Chem.* **97,** 48 (1992).
14. J. Rodriguez-Carvajal, in "Satellite Meeting on Powder Diffraction," p. 127. Abstracts of the XVth Conference of the International Union of Crystallography, Toulouse, 1990.
15. A. Ramnan, J. Gopalakrishnan, and C. N. R. Rao, *Mater. Res. Bull.* **16,** 169 (1981).
16. Y. Le Page, W. R. McKinnon, J. M. Tarascon, and P. Barboux, *Phys. Rev. B* **40,** 6810 (1989).
17. J. M. Tarascon, Y. Le Page, W. R. McKinnon, E. Tselepis, P. Barboux, B. G. Bagley, and R. Ramesh, *Mater. Res. Soc. Symp. Proc.* **156,** 317 (1989).
18. H. W. Zandbergen, W. A. Groen, F. C. Mijlhoff, G. Van Tendeloo, and S. Amelincks, *Physica C* **156,** 325 (1988).
19. M. Hervieu, C. Michel, D. Pelloquin, A. Maignan, and B. Raveau, *J. Solid State Chem.* **132,** 420 (1997).
20. B. Domengès, M. T. Caldes, M. Hervieu, A. Fuertes, and B. Raveau, *Microsc. Microanal. Microstruct.* **3,** 415 (1992).
21. M. T. Caldes, M. Hervieu, A. Fuertes, and B. Raveau, *J. Solid State Chem.* **98,** 45 (1992).
22. G. Van Tendeloo, B. Domengès, M. T. Caldes, M. Hervieu, and B. Raveau, *J. Solid State Chem.* **112,** 16 (1994).